

WS₂ Band Gap Renormalization Induced by Tomonaga Luttinger Liquid Formation in Mirror Twin Boundaries

Antonio Rossi^{1,2,3*†}, John C. Thomas^{1,3*†}, Johannes T. Kuchle^{1,4}, Elyse Barré¹, Zhuohang Yu^{5,6}, Da Zhou^{5,6}, Shalini Kumari^{5,6}, Hsin-Zon Tsai⁹, Ed Wong¹, Chris Jozwiak², Aaron Bostwick², Joshua A. Robinson^{5,6,7}, Mauricio Terrones^{5,6,7}, Archana Raja¹, Adam Schwartzberg¹, D. Frank Ogletree¹, Jeffrey B. Neaton^{3,9}, Michael F. Crommie^{3,9,10}, Francesco Allegretti⁴, Willi Auwärter⁴, Eli Rotenberg^{2*}, and Alexander Weber-Bargioni^{1,3*}

¹*Molecular Foundry, Lawrence Berkeley National Laboratory, Berkeley, CA 94720, United States of America*

²*Advanced Light Source, Lawrence Berkeley National Laboratory, Berkeley, CA 94720, United States of America*

³*Materials Sciences Division, Lawrence Berkeley National Laboratory, Berkeley, CA, United States of America*

⁴*Physics Department E20, Technical University of Munich, James-Franck-Str. 1, 85748 Garching, Germany*

⁵*Department of Materials Science and Engineering, The Pennsylvania State University, University Park, PA 16802 United States of America*

⁶*Center for Two-Dimensional and Layered Materials, The Pennsylvania State University, University Park, PA, 16802 United States of America*

⁷*Department of Physics and Department of Chemistry, The Pennsylvania State University, University Park, PA, 16802 United States of America*

⁸*Center for Advanced Mathematics for Energy Research Applications, Lawrence Berkeley National Laboratory, Berkeley, CA 94720, United States of America*

⁹*Department of Physics, University of California at Berkeley, Berkeley, CA, United States of America*

¹⁰*Kavli Energy Nano Sciences Institute, University of California Berkeley, Berkeley, CA, United States of America*

**afweber-bargioni@lbl.gov, arossi@lbl.gov, jthomas@lbl.gov*

†*These authors contributed equally.*

ABSTRACT

Tomonaga-Luttinger liquid (TLL) behavior in one-dimensional systems has been predicted and shown to occur at semiconductor-to-metal transitions within two-dimensional materials. Reports of mirror twin boundaries (MTBs) hosting a Fermi liquid or a TLL have suggested a dependence on the underlying substrate, however, unveiling the physical details of electronic contributions from the substrate require cross-correlative investigation. Here, we study TLL formation in MTBs within defectively engineered WS₂ atop graphene, where band structure and the atomic environment is visualized with nano angle-resolved photoelectron spectroscopy, scanning tunneling microscopy and scanning tunneling spectroscopy, and non-contact atomic force microscopy. Correlations between the local density of states and electronic band dispersion elucidated the electron transfer from graphene into a TLL hosted by MTB defects. We find that MTB defects can be substantially charged at a local level, which drives a band gap shift by ~ 0.5 eV.

One-dimensional (1D) systems in condensed matter physics provide unique insight into a variety of quasi particle excitations, including charge density waves (CDWs) that arise due to Peierls instabilities,^{1,2} lossless transport through electronic wires in topological edge states,³ quantum spin liquids,⁴ as well as more exotic phenomena such as Majorana modes in nanowires⁵ and the emergence of a Tomonaga-Luttinger liquid (TLL). The latter has been realized in both nanotubes and transition metal dichalcogenides (TMDs).⁶⁻¹⁷ These quasi particle excitations not only host new condensed matter physics phenomena but hold the promise to become major pillars of quantum electronics and quantum information applications.¹⁸ We show the capability to controllably create 1D confined systems and to directly observe TLL formation at its native length scale, which is key to understanding the governing principles behind such a strongly-correlated system.

The hallmarks of a TLL are the independent dispersion of charge and spin, fractional charge transport, and power law suppression of the density of states (DOS) near the Fermi energy (E_F).^{14-16,19} The formation of a TLL was first observed in 1D carbon nanotubes,^{8,9} where the conductance of bundled single-walled carbon nanotubes showed power law scaling with respect to bias voltage and temperature. This has since been extended to a number of 1D systems such as semiconductor single-channel wires, nanowires, organic conductors, and fractional quantum Hall edge channels.^{4,8,13,15,19-25} Recently, this phenomenon has also been shown to exist within 1D defects in two-dimensional (2D) TMDs at a plane of lattice points where the crystal structures on either side of the interface are mirrored, which defines a mirror twin boundary (MTB) within monolayer TMDs.¹⁴⁻¹⁶ MTBs have been predicted to exhibit metallic properties and to form out of sub-stoichiometric metal ($M = \text{Mo}, \text{W}$) or from depleted chalcogen ($X = \text{S}, \text{Se}, \text{Te}$) in MX_2 materials.^{22,26-28} TLL formation at MTB defects within TMDs adds to the the fascinating and vast array of material properties that 2D monolayer TMDs hold such as single photon emission, tunable band gaps, and strong spin-orbit coupling, to name a few.²⁹⁻³⁹ Zhu et al. have applied scanning tunneling microscopy and scanning tunneling spectroscopy (STM/STS) to directly map out the local density of states (LDOS) associated with TLLs,¹⁶ where measurements show a gap opening near E_F , a length dependence on the highest occupied and lowest unoccupied state band gap, and spin-charge dispersion observable in Fourier transform (FT) STS maps.^{14,15}

The role of the substrate for the formation of TLLs in MTBs has yet to be fully ascertained, and, in addition, a comprehensive understanding of the macroscopic band structure with the local electronic structure in TLL formation requires explanation. In order to address these questions, we engineer 1D defects into 2D WS_2 grown on graphene with tunable control over both length and density via a post-synthesis, *in-situ* approach. Measurement techniques cross-correlating STM/STS together with spatially- and nano angle-resolved photo emission spectroscopy (nARPES) help to give a broad range of information both on the electronic band structure of the system and the nature of the defects.⁴⁰ Non-contact atomic force microscopy (ncAFM) further enables structure identification of MTBs that host a TLL, where a metallic tip is functionalized with a CO molecule.^{28,41}

We report new insights into the role of the graphene substrate in TLL formation within 1D TMD MTB heterostructures. Two 1D defect symmetries are unambiguously identified, where their controlled introduction enables TLL formation. Exclusive doping (charge transfer) from graphene into an MTB gives on the order of $\sim 4-5$ electrons per MTB, which brings the E_F of graphene near the Dirac point reducing its screening power and, therefore, increasing the electron-electron interaction in the MTBs. We also observe an atomically localized band gap renormalization over the MTB/TLL systems, with indications of the conduction band taking part in TLL formation.

In order to study 1D MTB defects that may host a TLL, we perform STM/STS studies on both unmodified WS_2 , grown epitaxially via chemical vapor deposition (CVD) on a graphene/SiC substrate, and the same sample after Ar^+ sputtering and annealing *in-situ* to induce defectivity.⁴²⁻⁴⁴ Comparative results of low-energy sputtering in contrast to a low-temperature anneal are shown (Fig. 1 (a-b)). As-grown samples are not significantly modified by annealing up to 250 °C, while chalcogen vacancies (V_S) start to form at 600 °C.³⁷ Low-energy Ar^+ sputtering at chalcogen creation sample temperatures

(SA_{step}) greatly increases the density of V_S and MTB defects (see Supplementary Notes 1 and 2 and Supplementary Figs. 1 and 2 for both density calculations and SRIM simulations) compared to only annealing. Post SA_{step} annealing at 600 °C (SAA_{step}) substantially reduces point defect density, where MTBs with increased length ($L_{SA_{step}} = 3.37 \pm 2.87$ nm, $L_{SAA_{step}} = 8.75 \pm 4.01$ nm) are formed (see Supplementary Fig. 1).

We confirm local structure via ncAFM performed with a functionalized CO tip in Fig. 1 (c and d). Under the conditions of chalcogen depletion and excess metal, the asymmetric mirror glide boundary (AMGB) and the symmetric mirror twin boundary (SMTB), amongst other possible formations, are predicted to be favorable in TMDs,^{22,27,45} where we measure the formation of both AMGB and SMTB defects under the conditions described (see Supplementary Fig. 3) that corresponds to predicted structures. As ncAFM frequency shifts are not affected by the electronic structure changes near E_F ,²⁸ the atomically-resolved images obtained of SMTB in WS_2 are described by a WS_2 edge sharing chalcogen point sites, and, in addition, the acquired AMGB is characterized by an edge shifted by half of a lattice spacing ($a = 0.315$ nm) with W bonded to four sulfur atoms across the MTB (see Supplementary Fig. 4).⁴⁶ It may be important to note that while MTBs have been more extensively studied in MoS_2 and $MoSe_2$, high formation energy in WS_2 has hindered atomic-scale investigations of MTBs. We are able to take advantage of sulfur reduction techniques coupled with tandem atomic-scale measurements. Upon further investigation with STS, the two types of defects introduced during both SA_{step} and SAA_{step} are verified to be MTBs and V_S , as detailed in Fig. 1 (e). Here, the band gap of surrounding WS_2 is measured to be on the order of 2.5 eV and V_S shows deep unoccupied defect states split by spin-orbit coupled W d states, which is consistent with previously measured values.³⁷ Conversely, MTBs show a semiconducting band gap between the highest occupied state (HOS) and lowest unoccupied state (LUS) on the order of 100 meV.

In order to better investigate the physics of the MTB bandgap formed in WS_2 , we make use of both point STS and differential conductance mapping, which are powerful tools for screening defects.^{28,37,47} Electronic band-edge state differential conductance maps, acquired by dI/dV imaging (Fig. 2 (a-f)), at the LUS (ψ_-) and the HOS (ψ_+) are spatially out-of-phase for the SMTB case, and are a spatially in-phase for an AMGB. Additionally, the number of orbital nodes changes as a function of bias for both the AMGB and the SMTB. This 1D particle-in-a-box behavior, which has been demonstrated for both types of defects in other TMDs, such as $MoSe_2$ and MoS_2 , shows an increasing number of nodes moving further past the LUS (with decreasing period) and a decreasing number of nodes moving below the HOS (with increased period) for the SMTB or the reverse behavior for the AMGB,^{14,16} which is consistent with our measurements. We find that the nodal periodicity at the HOS and LUS for a measured SMTB structure (Fig. 2 (a-b)) is near 2 nm and 1.5 nm, respectively, which is far above the lattice constant of 0.315 nm. Additionally, the measured periodicity for the inspected AMGB structure is 0.5 nm (Fig. 2 (d-e)) at both the HOS and the LUS, which is not within an integer relationship with the lattice parameter of WS_2 . Supplemental Fig. 5 and 6 further show conductance maps as a function of energy both below HOS and above the LUS for both structures, where the presence of a neighboring V_S does not show significant hybridization with an SMTB across measured energy regimes. We also highlight nodal increase as a function of bias in Fig. 2 (c), where the number of nodes moves from 6 at the LUS up to 10 nodes at 0.4 eV before nearing the CBM of WS_2 for the SMTB. This is also shown for an AMGB in Fig. 2 (f), where 8 nodes are measured at the HOS and 9 nodes are measured at -0.3 eV. A dense ($1 \times 128 \times 500$) linescan of point spectroscopy is captured in Supplementary Fig. 7, where nodes increase by an integer number as the bias is swept from below the HOS to above the LUS for an SMTB, which is depicted both spatially and in Fourier space. Here, the HOS has 4 nodes and the LUS has 5, increasing up to 10 nodes at 0.31 eV. As low-energy excitations are not Fermi liquid quasiparticles in TLL theory, the spin- and charge-density waves exhibit different dispersions and velocities, denoted as v_s and v_c , respectively. Their ratio can be experimentally measured in the FT-STs measurement as $K_c = v_s/v_c$, where K_c is the Luttinger parameter. From our FT-STs, we extract a K_c of 0.5, which is consistent with previously acquired values on other TMD systems.^{14,16} Band gap (E_{gap}) as a function of length is shown in Supplementary Fig. 8, where E_{gap} is dependent upon length (L), scaling linearly with L^{-1} . This behaviour stands in contrast to Peierls

instability, where the E_{gap} is constant in the CDW case and does not exhibit a length dependence.¹⁴ Finally, we also look at the DOS measured in topographic STM images. TLL nodal oscillations are indistinguishable above CBM of WS₂, however, a measure of signal intensity as a function of distance is feasible. Here, electron density is expected to decay according to K_c as $\rho \sim x^{-K_c}$,¹⁵ where the DOS (ρ) measured under constant-current as a function of distance (x), in nanometers, is shown in Supplementary Fig. 9. The fitted exponential function yields a value of 0.5 that is well-matched to the values obtained in the FT-STs and in agreement with previously measured MTBs that host a TLL.¹⁴⁻¹⁶ Overall, we identify the TLL properties of these defects by observing a Luttinger parameter of 0.5, measuring an E_{gap} opening near E_F , identifying an E_{gap} dependence on MTB length, visualizing 1D particle in a box behavior, and extracting evidence of spin-charge separation.

We next perform nARPES to directly visualize the crystal band dispersion. The sub- μm probe in nARPES offers a spatial resolution capable of capturing the local inhomogeneity in the sample. Fig. 3 showcases the as-measured band structure of the unmodified crystal versus the sample exposed to Ar⁺ bombardment. The two spectra are collected from the same sample, where a small region is found to be unaffected by the SA_{step} , due to sample holder shadowing during preparation. The spectrum obtained from the non-defective structure is displayed in Fig. 3 (a). It is collected along the Γ -K direction. Graphene and WS₂ keep epitaxial registry, therefore WS₂ also has the same crystal orientation.⁴⁸ A sketch of the two Brillouin zones (BZ) (graphene in black, WS₂ in green) is highlighted in the inset of Fig. 3 (a). Graphene exhibits sharp bands with the $E_F \sim 400$ meV above the Dirac point. This is consistent with graphene prepared from thermal decomposition of SiC, where the carbon-rich buffer layer between graphene and SiC substrate creates an electric dipole at the interface affecting the chemical potential of graphene.⁴⁹ Such a native gating also affects the WS₂ band, whose top of the valence band appears to be ~ 1.48 eV below the E_F .⁴⁸ The local maximum at Γ appears below the maximum at K, confirming the monolayer nature of the TMD.⁵⁰ The SA_{step} deeply affects the bands of WS₂. Fig. 3 (b) shows the spectrum obtained from the region with high defect density due to the SA_{step} . A substantial band gap renormalization is observed, where both the magnitude and chemical potential position are affected. The WS₂ occupied electron bands are shifted upwards by ~ 500 meV. The position of the top of the valence band is further confirmed by the spectrum collected with linear vertical polarization (see Supplementary Fig. 10). The graphene bands are also shifted up, although not by the same magnitude, with a subsequent change in the doping level. This is clear analyzing the Dirac bands collected near the K point of the graphene BZ along the direction highlighted in red within the inset of panel (a) (Fig. 3 (c and d)). The momentum distribution curves (MDCs), collected at the E_F (Fig. 3 (e and f)) can be fit with two Lorentzian functions. The position of their peaks defines a distance that approximates the diameter of the circle fitting the Fermi surface of graphene. Using Luttinger theorem,^{51,52} it is possible to extract the doping level being $n_p = 1.2 \times 10^{13} \text{ cm}^{-2}$ and $n_d = 2.5 \times 10^{12} \text{ cm}^{-2}$ for the as-grown and defective crystal, respectively (Fig. 3 (c-f)). The unmodified doping level agrees well with the value found in literature.⁵¹ From these values and locally-measured defect densities (Supplementary Fig. 1 and Supplementary Note 2), we are able to determine that each MTB hosts 3-8 electrons ($0.021 \pm 0.009 \frac{MTB}{nm^2}$). Our Monte Carlo calculations further suggest that our sample treatment does not have a direct impact on graphene (Supplementary Fig. 2). As a matter of fact, the presence of defects in graphene would open a gap at the Dirac point caused by an alteration of the system symmetry rather than shifting its chemical potential.⁵³ The shift of the Dirac point in graphene is the result of charge transfer from graphene to the newly formed MTBs in WS₂. The chemical potential difference with respect to the as-grown crystal does not match the magnitude observed for WS₂. Our findings suggest that graphene plays a significant role in the formation of a TLL, both donating charge to the newly formed defects and providing a weaker electronic screening due to the lower carrier density near neutrality point. This, overall, increases the electron-electron interaction strength in the TMD.

In Fig. 3 (g), we analyze the energy distribution curves (EDC) crossing the top of the valence band (vertical dashed line in Fig. 3 (a-b)) by overlapping the EDCs with the STS curves collected from the unmodified crystal, a single sulfur vacancy, and an MTB formed on the TMD. The band shift is caused mostly by a band gap renormalization related to the presence of the MTB as opposed to isolated sulfur

vacancies. Indeed, the onset of the valence band displayed by the STS obtained from the sulfur vacancy (dashed green line) does not match the onset of the valence band extracted by the EDC taken from Fig. 3 (b). Conversely, the STS curve obtained from the 1D MTB (dark red line) displays the onset of the valence band matching the EDC from nARPES data taken after the SA_{step} (light red line). The blue lines show the EDC and STS comparison from the pristine structure, where in this case the alignment between the two curves is well-matched at the expected onset of the valence band. This behavior is additionally measured with spatially-localized STS acquisition in Fig. 4, where a shift in the VBM is seen approaching an MTB with an STM tip. The measured onsets of the VBM (-1.16 ± 0.04 eV) and the CBM (0.74 ± 0.09 eV) was measured locally with STS, which corresponds with the appearance of the HOS and LUS. The relative shift of the VBM is +530 meV (CBM is shifted by -80 meV) and is further depicted in Fig. 4 (a), which matches well to the band structure acquired by nARPES. Both nARPES measurements and STS highlight the importance in choice of substrate to determine the electronic properties of 1D defects in TMDs. Where other findings have shown a substrate dependence,¹⁵ cross-correlated measurements made in this report are able to directly visualize the E_F position related to the presence of MTBs over graphene. W $4f$ and S $2p$ core levels in Supplementary Fig. 11 show both core levels are rigidly shifted to lower binding energy in a similar fashion as the bands in the valence region. This suggests that the band gap renormalization is overall electrostatically driven. W and S peak fitting upon MTB formation displays a weaker component that is further shifted towards a lower binding energy of an additional few hundreds of meV due to the local chemical environment.

This work presents a new, controllable way to create MTBs in WS_2 epitaxially grown on graphene is presented. We show how MTBs host a TLL, in which spectroscopic and topological signature is shown via STM/STS and ncAFM. A band gap opening of roughly 100 meV is observed near the E_F confirming the correlated nature of the electronic state inside the 1D defect. We demonstrated the formation of two kinds of MTBs, AMGB and SMTB, which display similar spectroscopic features but a distinct spatial difference in conductance image mapping. By means of nARPES, we were able to correlate scanning probe spectroscopic MTB features to the band structure of the crystal. We observed how defective states behave as an acceptor of graphene electrons and that they cause a massive band gap renormalization of WS_2 . The same effect is reflected on core levels where we observe a similar chemical shift in binding energies.

Encoding information with two different quantum degrees of freedom across 1D structures can have immediate relevance for quantum information processing, where application of such materials has yet to be manifested in functional devices. Additionally, electron transport across semiconductor to metal transitions may be beneficial in ultrafast electronic systems. Here, we provide a step-by-step approach to produce 1D metallic structures within a 2D semiconducting material, which holds relevance in atomic-scale tailorable systems and electronic modification at the nanoscale. We further anticipate engineered TMD materials to be relevant in spin-polarized measurements, charge state effects, and spin transport.

1 METHODS

1.1 Scanning probe microscopy (SPM) measurements

All measurements were performed with a Createc GmbH scanning probe microscope operating under ultrahigh vacuum (pressure $< 2 \times 10^{-10}$ mbar) at liquid helium temperatures ($T < 6$ K). Either etched tungsten or platinum iridium tips were used during acquisition. Tip apexes were further shaped by indentations into a gold substrate. STM images are taken in constant-current mode with a bias applied to the sample. STS measurements were recorded using a lock-in amplifier with a resonance frequency of 683 Hz and a modulation amplitude of 5 mV.

In ncAFM measurements, a qPlus quartz-crystal cantilever was used (resonance frequency, $f_0 \approx 30$ kHz; spring constant, $k \approx 1800$ N/m; quality factor, $Q > 18,000$; and oscillation amplitude, $A \approx 1$ Å).³⁶ The metallic tip was functionalized with a CO molecule for enhanced resolution.⁴¹

1.2 Angle-resolved photoemission spectroscopy (ARPES) measurements

ARPES experiments were performed in ultra high vacuum at $T = 6\text{K}$ at beamline 7.0.2 (MAESTRO) at the Advanced Light Source. The beam-spot size was $\approx 1\ \mu\text{m}$. The photon energy for the valence band structure is $h\nu = 150\ \text{eV}$ and $h\nu = 350\ \text{eV}$ for core levels. The XPS curve-fitting analysis was performed using a convolution of Doniach-Sunjić and Gaussian line shapes superimposed on a background built of a constant, a linear component, and a step-function. For each S $2p$ spin-orbit doublet, a spin-orbit splitting of $1.2\ \text{eV}$ and a branching ratio $I(2p_{3/2}) : I(2p_{1/2}) = 2 : 1$ (defined in terms of peak areas) were used. The W $4f$ spin-orbit doublets were fit using individual components with a spin-orbit splitting of $2.2\ \text{eV}$, to take into account non-linearities.

1.3 Sample preparation

Monolayer islands of WS_2 were grown on graphene/SiC substrates with an ambient pressure CVD approach. A monolayer graphene (MLG)/SiC substrate with $10\ \text{mg}$ of WO_3 powder on top was placed at the center of a quartz tube, and $400\ \text{mg}$ of sulfur powder was placed upstream. The furnace was heated to $900\ ^\circ\text{C}$ and the sulfur powder was heated to $250\ ^\circ\text{C}$ using a heating belt during synthesis. A carrier gas for process throughput was used (Ar gas at $100\ \text{sccm}$) and the growth time was $60\ \text{min}$. The CVD grown $\text{WS}_2/\text{MLG}/\text{SiC}$ was further annealed *in vacuo* at $400\ ^\circ\text{C}$ for $2\ \text{hours}$.

Monolayer WS_2 was sputtered with an argon ion gun (SPECS, IQE 11/35) that operated at $0.1\ \text{keV}$ energy with 60° off-normal incidence at a pressure of $5 \times 10^{-6}\ \text{mbar}$ and held at $600\ ^\circ\text{C}$. A rough measure of current ($0.6 \times 10^{-6}\ \text{A}$) enabled the argon ion flux to be estimated at ($1.5 \times 10^{13}\ \frac{\text{ions}}{\text{cm}^2\text{s}}$), where the sample was irradiated for up to $30\ \text{seconds}$.

Samples were transferred from the STM to the nARPES chamber using an Ar suitcase that prevented air exposure to enable cross-correlative studies without risking sample degradation.

Data availability

All data needed to evaluate the conclusions exhibited are present in the paper and/or the supplemental information.

Code availability

Software used for analysis are either presented in the supplemental information or can be provided upon reasonable request from the authors.

Acknowledgements

The authors thank Nino Hatter and Sebastian Baum from CreaTec Fischer & Co. GmbH for helpful discussions. This work was supported as part of the Center for Novel Pathways to Quantum Coherence in Materials, an Energy Frontier Research Center funded by the U.S. Department of Energy, Office of Science, Basic Energy Sciences. Work was performed at the Molecular Foundry and at the Advanced Light Source, which was supported by the Office of Science, Office of Basic Energy Sciences, of the U.S. Department of Energy under contract no. DE-AC02-05CH11231. S.K and J.A.R. acknowledge support from the National Science Foundation Division of Materials Research (NSF-DMR) under awards 2002651 and 2011839. J.T.K and F.A. acknowledge financial support by the Deutsche Forschungsgemeinschaft (DFG) through the TUM International Graduate School of Science and Engineering (IGSSE), GSC 81.

Author Contributions

A.R., J.C.T., and A.W.-B. conceived and carried out the experiments. A.R., J.C.T., and J.T.K carried out nARPES/XPS measurements with the assistance of C.J., A.B., and E.R. E.B. and J.C.T. contributed to SRIM/TRIM simulations. A.R., J.C.T., and J.T.K. carried out ncAFM measurements with the assistance

of H.-Z.T. and M.F.C. A.R., J.C.T., and J.T.K. performed all STM/STS experiments with additional contributions from A.R., E.W., A.S., D.F.O., F.A., W.A., and A.W.-B. A.R. and J.C.T. performed all nARPES related data analysis with support from C.J., A.B., and E.R. A.R. and J.C.T. performed all ncAFM, STM, and STS related data analysis with support from A.R., E.W., A.S., D.F.O., J.B.N., M.F.C., F.A., W.A., and A.W.-B. Z.Y., T.Z., S.K., J.A.R. and M.T. synthesized the samples. All authors discussed the results and contributed towards the manuscript.

Competing interests

The authors declare that they have no competing interests.

REFERENCES

- [1] Wang, L. et al. Direct observation of one-dimensional Peierls-type charge density wave in twin boundaries of monolayer MoTe₂. *ACS Nano* **14**, 8299 (2020).
- [2] Peierls, R. & Peierls, R. E. *Quantum theory of solids*. (Oxford Univ. Press, 1955).
- [3] Schindler, F. et al. Higher-order topology in bismuth. *Nat. Phys.* **14**, 918 (2018).
- [4] Kim, B. J. et al. Distinct spinon and holon dispersions in photoemission spectral functions from one-dimensional SrCuO₂. *Nat. Phys.* **2**, 397 (2006).
- [5] Mourik, V. et al. Signatures of Majorana fermions in hybrid superconductor-semiconductor nanowire devices. *Science* **336**, 1003 (2012).
- [6] Tomonaga, S.-I. Remarks on Bloch's method of sound waves applied to many-fermion problems. *Prog. Theor. Phys.* **5**, 544 (1950).
- [7] Luttinger, J. M. An exactly soluble model of a many-fermion system. *J. Math. Phys.* **4**, 1154 (1963).
- [8] Bockrath, M. et al. Luttinger-liquid behaviour in carbon nanotubes. *Nature* **397**, 598 (1999).
- [9] Ishii, H. et al. Direct observation of Tomonaga-Luttinger-liquid state in carbon nanotubes at low temperatures. *Nature* **426**, 540 (2003).
- [10] Lee, J. et al. Real space imaging of one-dimensional standing waves: Direct evidence for a Luttinger liquid. *Phys. Rev. Lett.* **93**, 166403 (2004).
- [11] Auslaender, O. M. et al. Tunneling spectroscopy of the elementary excitations in a one-dimensional wire. *Science* **295**, 825 (2002).
- [12] Auslaender, O. M. et al. Spin-charge separation and localization in one dimension. *Science* **308**, 88 (2005).
- [13] Jompol, Y. et al. Probing spin-charge separation in a Tomonaga-Luttinger liquid. *Science* **325**, 597 (2009).
- [14] Jolie, W. et al. Tomonaga-Luttinger liquid in a box: Electrons confined within MoS₂ mirror-twin boundaries. *Phys. Rev. X* **9**, 011055 (2019).
- [15] Xia, Y. et al. Charge density modulation and the Luttinger Liquid state in MoSe₂ mirror twin boundaries. *ACS Nano* **14**, 10716 (2020).
- [16] Zhu, T. et al. Imaging gate-tunable Tomonaga-Luttinger liquids in 1H-MoSe₂ mirror twin boundaries. *Nat. Mater.* **21**, 748 (2022).

- [17] Jia, J. et al. Tuning the many-body interactions in a helical Luttinger liquid. *Nat. Commun.* **13**, 6046 (2022).
- [18] Keimer, B. & Moore, J. E. The physics of quantum materials. *Nat. Phys.* **13**, 1045 (2017).
- [19] Hashisaka, M. & Fujisawa, T. Tomonaga–Luttinger-liquid nature of edge excitations in integer quantum hall edge channels. *Phys. Rev.* **3**, 32 (2018).
- [20] Liu, H. et al. Dense network of one-dimensional midgap metallic modes in monolayer MoSe₂ and their spatial undulations. *Phys. Rev. Lett.* **113**, 066105 (2014).
- [21] Ma, Y. et al. Angle resolved photoemission spectroscopy reveals spin charge separation in metallic MoSe₂ grain boundary. *Nat. Commun.* **8**, 14231 (2017).
- [22] Lehtinen, O. et al. Atomic scale microstructure and properties of Se-deficient two-dimensional MoSe₂. *ACS Nano* **9**, 3274 (2015).
- [23] Park, J., Xue, K.-H., Mouis, M., Triozon, F.M.C., & Cresti, A. Electron transport properties of mirror twin grain boundaries in molybdenum disulfide: Impact of disorder. *Phys. Rev. B* **100**, 235403 (2019).
- [24] Ma, Y. et al. Metallic twin grain boundaries embedded in MoSe₂ monolayers grown by molecular beam epitaxy. *ACS Nano* **11**, 5130 (2017).
- [25] Du, X. et al. Crossed Luttinger liquid hidden in a quasi-two-dimensional material. *Nat. Phys.* **19**, 40 (2023).
- [26] Gibertini, M. & Marzari, N. Emergence of one-dimensional wires of free carriers in transition-metal-dichalcogenide nanostructures. *Nano Lett.* **15**, 6229 (2015).
- [27] Batzill, M. Mirror twin grain boundaries in molybdenum dichalcogenides. *J. Condens. Matter Phys.* **30**, 493001 (2018).
- [28] Barja, S. et al. Charge density wave order in 1D mirror twin boundaries of single-layer MoSe₂. *Nat. Phys.* **12**, 751 (2016).
- [29] Lin, Z. et al. Defect engineering of two-dimensional transition metal dichalcogenides. *2D Materials* **3**, 022002 (2016).
- [30] Sangwan, V. K. & Hersam, M. C. Electronic transport in two-dimensional materials. *Annu. Rev. Phys. Chem.* **69**, 299 (2018).
- [31] Shimazaki, Y. et al. Strongly correlated electrons and hybrid excitons in a moiré heterostructure. *Nature* **580**, 472 (2020).
- [32] Wang, L. et al. Correlated electronic phases in twisted bilayer transition metal dichalcogenides. *Nat. Mater.* **19**, 861 (2020).
- [33] Manzeli, S., Ovchinnikov, D., Pasquier, D., Yazyev, O. V., & Kis, A. 2D transition metal dichalcogenides. *Nat. Rev. Mater.* **2**, 1 (2017).
- [34] Li, C. et al. Engineering graphene and TMDs based van der waals heterostructures for photovoltaic and photoelectrochemical solar energy conversion. *Chem. Soc. Rev.* **47**, 4981 (2018).
- [35] Ugeda, M. M. et al. Observation of topologically protected states at crystalline phase boundaries in single-layer WSe₂. *Nat. Commun.* **9**, 3401 (2018).
- [36] Schuler, B. et al. Electrically driven photon emission from individual atomic defects in monolayer WS₂. *Sci. Adv.* **6**, eabb5988 (2020).

- [37] Schuler, B. et al. Large spin-orbit splitting of deep in-gap defect states of engineered sulfur vacancies in monolayer WS₂. *Phys. Rev. Lett.* **123**, 076801 (2019).
- [38] Mitterreiter, E. et al. Atomistic positioning of defects in helium ion treated single-layer MoS₂. *Nano Lett.* **20**, 4437 (2020).
- [39] Mitterreiter, E. et al. The role of chalcogen vacancies for atomic defect emission in MoS₂. *Nat. Commun.* **12**, 3822 (2021).
- [40] Kastl, C. et al. Effects of defects on band structure and excitons in WS₂ revealed by nanoscale photoemission spectroscopy. *ACS Nano* **13**, 1284 (2019).
- [41] Schuler, B. et al. How substitutional point defects in two-dimensional WS₂ induce charge localization, spin-orbit splitting, and strain. *ACS Nano* **13**, 10520 (2019).
- [42] Kastl, C. et al. The important role of water in growth of monolayer transition metal dichalcogenides. *2D Materials* **4**, 021024 (2017).
- [43] Kastl, C. et al. Multimodal spectromicroscopy of monolayer WS₂ enabled by ultra-clean van der waals epitaxy. *2D Materials* **5**, 045010 (2018).
- [44] Ma, L. et al. Tailoring the optical properties of atomically-thin WS₂ via ion irradiation. *Nanoscale* **9**, 11027 (2017).
- [45] Komsa, H.-P. & Krasheninnikov, A. V. Engineering the electronic properties of two-dimensional transition metal dichalcogenides by introducing mirror twin boundaries. *Adv. Electron. Mater.* **3**, 1600468 (2017).
- [46] Lin, J., Pantelides, S. T., & Zhou, W. Vacancy-induced formation and growth of inversion domains in transition-metal dichalcogenide monolayer. *ACS Nano* **9**, 5189 (2015).
- [47] Thomas, J. C. et al. Autonomous scanning probe microscopy investigations over WS₂ and Au{111}. *npj Comput. Mater.* **8**, 99 (2022).
- [48] Forti, S. et al. Electronic properties of single-layer tungsten disulfide on epitaxial graphene on silicon carbide. *Nanoscale* **9**, 16412 (2017).
- [49] Ristein, J., Mammadov, S., & Seyller, T. Origin of doping in quasi-free-standing graphene on silicon carbide. *Phys. Rev. Lett.* **108**, 246104 (2012).
- [50] Kuc, A., Zibouche, N., & Heine, T. Influence of quantum confinement on the electronic structure of the transition metal sulfide TS₂. *Phys. Rev. B* **83**, 245213 (2011).
- [51] Bostwick, A., Ohta, T., Seyller, T., Horn, K., & Rotenberg, E. Quasiparticle dynamics in graphene. *Nat. Phys.* **3**, 36 (2007).
- [52] Rosenzweig, P., Karakachian, H., Marchenko, D., üster, K. K., & Starke, U. Overdoping graphene beyond the van Hove singularity. *Phys. Rev. Lett.* **125**, 176403 (2020).
- [53] Kot, P. et al. Band dispersion of graphene with structural defects. *Phys. Rev. B* **101**, 235116 (2020).

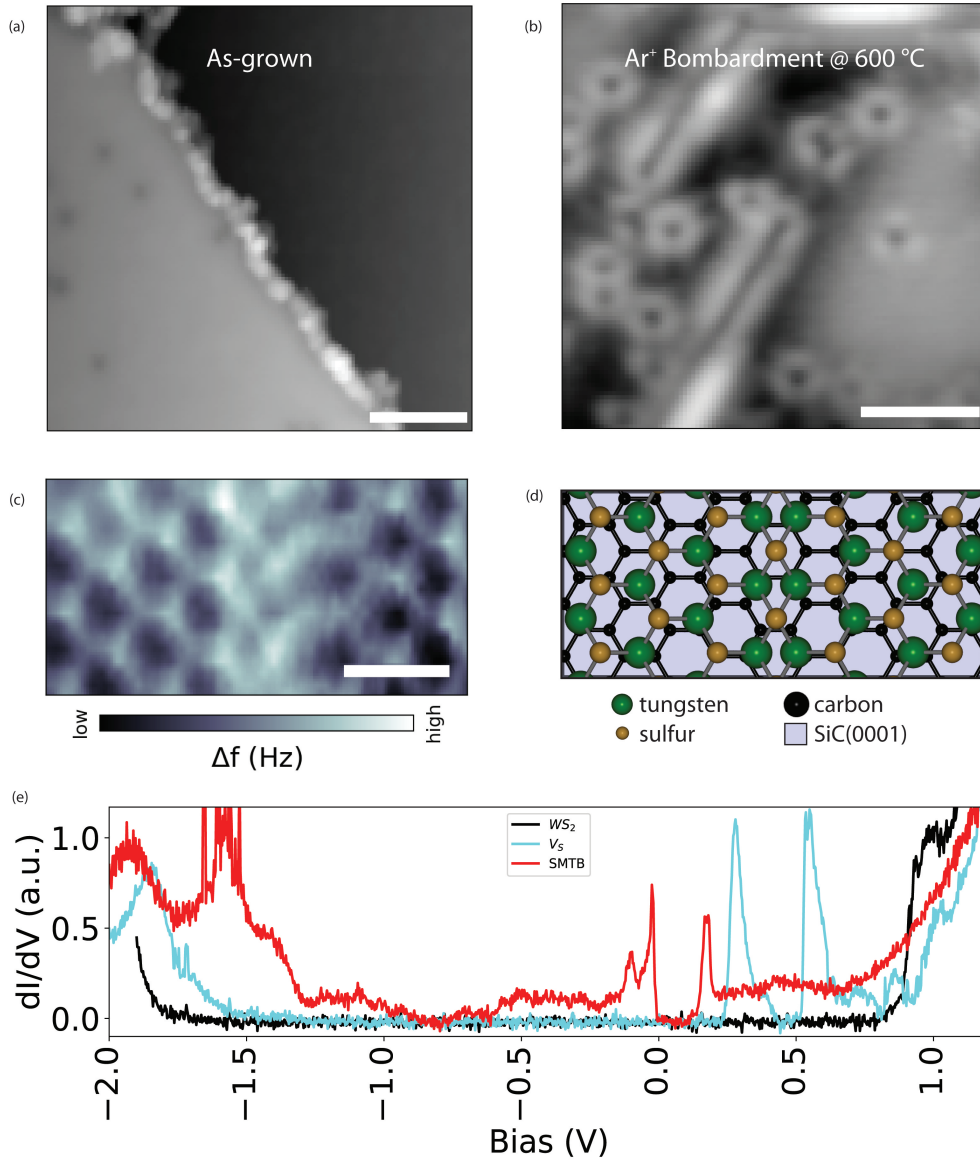


Fig. 1: **WS₂ Defect Introduction.** (a) Scanning tunneling micrograph depicting pristine WS₂ before Ar⁺ bombardment ($I_{tunnel} = 30$ pA, $V_{sample} = 1.2$ V). Scale bar, 10 nm. (b) After the pristine sample is heated and exposed to an Ar⁺ sputter ($I_{tunnel} = 30$ pA, $V_{sample} = 1.2$ V), both V_S and MTBs are present. Scale bar, 2 nm. (c) Lattice structure is measured by n-AFM ($V_{sample} = 0.0$ V), with a CO-functionalized tip, which showcases the SMTB that is placed next to a structural schematic of (d) of the MTB. Scale bar, 0.25 nm. (e) Point spectroscopy, in the form of the LDOS, for unmodified WS₂, V_S, and an SMTB.

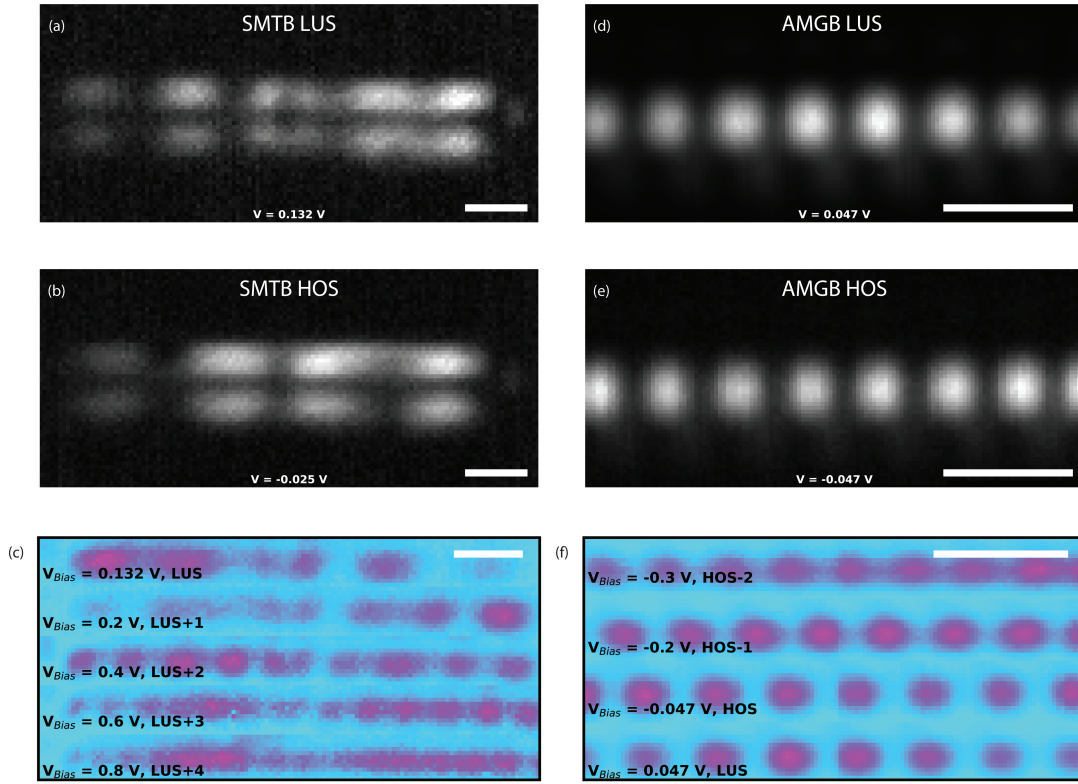


Fig. 2: **LDOS Mapping.** Conductance maps ($V_{modulation} = 5$ mV) performed across an SMTB show dual-line orbital behavior at (a) 0.132 eV (LUS) and (b) -0.025 eV (HOS) that is spatially out of phase. (c) Accumulated conductance maps across a single-line of the SMTB ($V_{modulation} = 5$ mV) are further shown as a function of bias, where the number of nodes increase as bias voltage is increased. Scale bars, 1 nm. Conductance maps (dI/dV) of the (d) 0.047 eV (LUS) and (e) -0.047 eV (HOS) that are spatially in phase within a single-line AMGB. (f) Compiled conductance maps ($V_{modulation} = 5$ mV) across the single-line AMGB are further shown, where the number of nodes decreases as the voltage is increased.

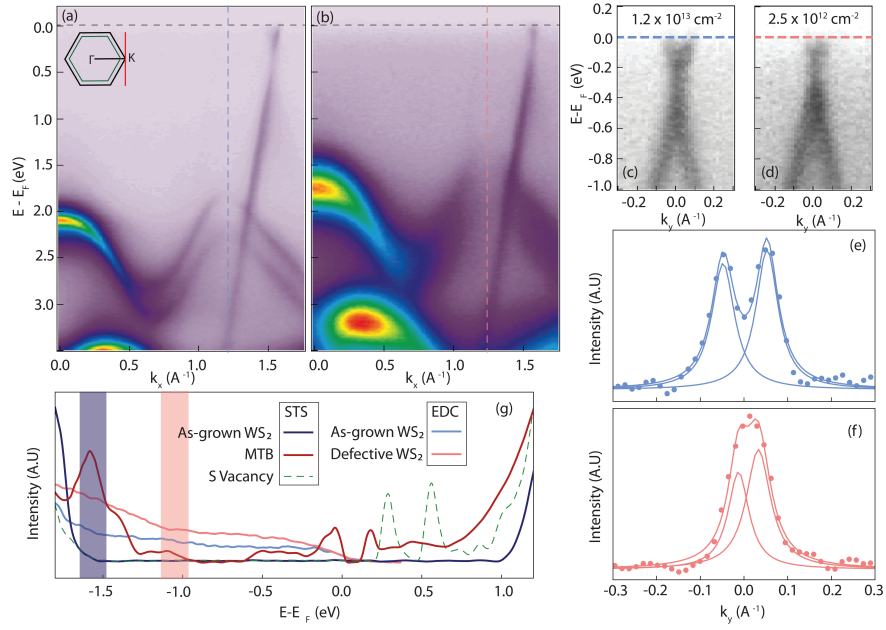


Fig. 3: nARPES Band Structure Comparison. (a) Unmodified and (b) defective band structure of WS₂ on graphene. The inset displays the WS₂ (green) and the graphene (black) BZ. The spectra are collected along the Γ -K orientation. nARPES spectra of as-grown (c) and defective (d) crystals that are collected along the red line of the inset in panel (a), with respective MDCs at the E_F shown in (e) and (f). (g) EDCs overlapped with STS from unmodified and defective WS₂. Dark blue and dark red are the STS signals collected on pristine WS₂ and on an MTB, respectively. Dashed green is the STS spectrum collected on an isolated sulfur vacancy. The light blue and light red lines are the EDCs collected at the K point of the BZ (dashed vertical lines in panels (a) and (b) respectively).

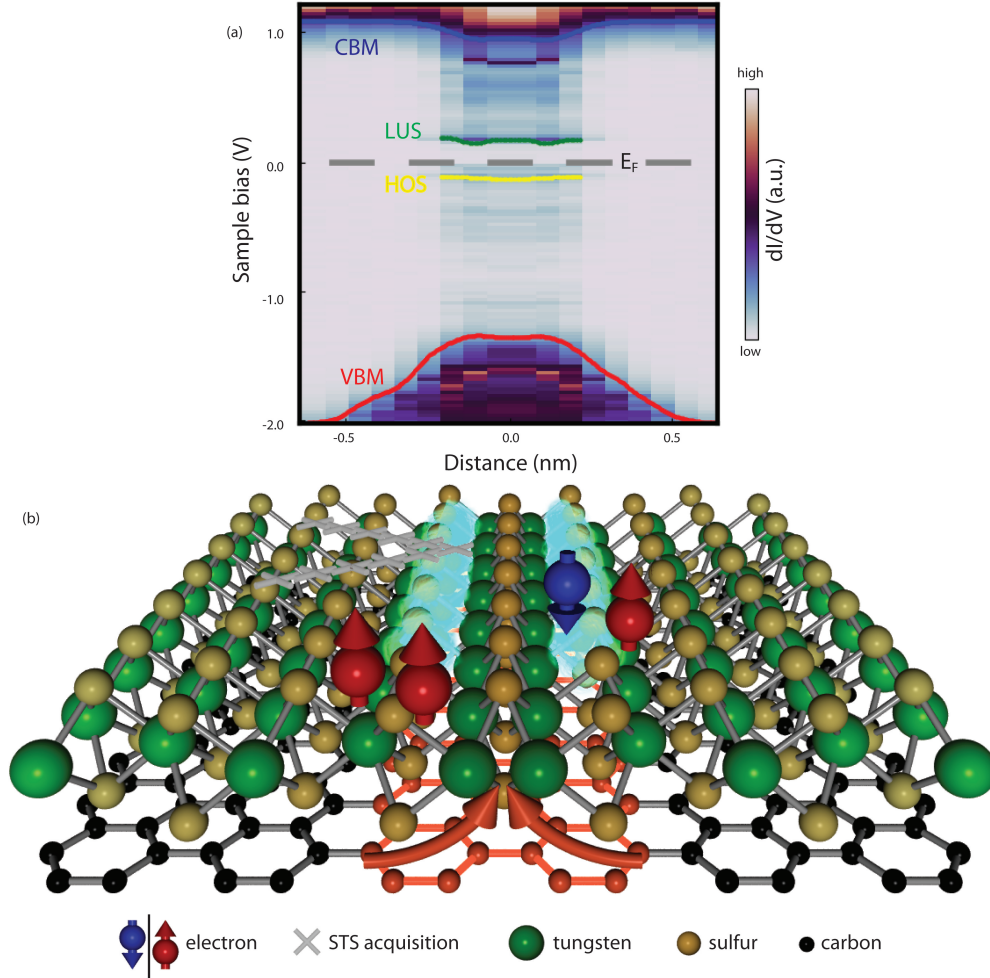


Fig. 4: **Tomonaga Luttinger Liquid Spatial Dependence.** (a) LDOS spectra collected from pristine WS₂ to an MTB ($V_{modulation} = 5$ mV, $I_{set} = 150$ pA) and then recorded in reverse. The as-measured VBM, CBM, HOS, and LUS are highlighted with relative positions to E_F . (b) The process of charge transfer from graphene into an MTB that is able to host highly correlated electron states is depicted, where the E_F of graphene is shifted and locally modified due to the presence of an MTB.

Supplemental Information for WS₂ Band Gap Renormalization Induced by Tomonaga Luttinger Liquid Formation in Mirror Twin Boundaries

SUPPLEMENTARY NOTES

1| Ar⁺ sputtering and SRIM simulations

Monte Carlo simulations based on The Stopping and Range of Ions in Matter, SRIM simulations,¹ were used to evaluate preparation conditions using Ar⁺ bombardment. The Transport of Ions in Matter (TRIM) calculation, which assumes amorphous targets, with 50,000 ions was determined to be sufficient for simulation convergence; between simulating 20,000 and 50,000 ions, the variation in the number of vacancies created was less than 2% for all possible atomic vacancies. The Ar⁺ energy was set to 0.1 keV to gauge angle dependence and fixed at an angle of 60° to gauge energy dependence, where these values were chosen to be used experimentally. We set the height of WS₂ to 0.72 nm, the height of graphene to 0.34 nm, and the height of SiC to 30 nm.^{2,3} Density, displacement energy, and surface binding energy values were matched to literature values.⁴⁻⁶

Using the estimated argon flux of $1.5 \times 10^{13} \frac{\text{ions}}{\text{cm}^2 \cdot \text{s}}$ at 30 seconds of irradiation, we obtain a value of $4.5 \frac{\text{ions}}{\text{nm}^2}$. Each ion is predicted to induce $3 V_S$, or $13.5 \frac{V_S}{\text{nm}^2}$. Considering the local measurement of $0.168 \pm 0.052 \frac{V_S}{\text{nm}^2}$ and MTB formation of $0.021 \pm 0.009 \frac{\text{MTB}}{\text{nm}^2}$ with a length of 3.37 ± 2.87 nm (2 missing sulfur per 0.315 nm in symmetric mirror twin boundary (SMTB) and the asymmetric mirror glide boundary (AMGB)), we extract an upper bound value of $1.4 \frac{S_{\text{missing}}}{\text{nm}^2}$ and lower bound value of $0.2 \frac{S_{\text{missing}}}{\text{nm}^2}$. We use simulation results to estimate defect creation and local measurements to approximate defect density.

2| Defect analysis

An object class can be instantiated within Python, where each image can be loaded for analysis with a given size (nm). Defects are selected initially by inspection, and local minima or maxima are calculated within a given pixel range. Each selected defect is then cross-checked and input into a graph, where density can be calculated by the number of defects within a the given area, assuming an equal N×N image.

```
class node(object):
    def __init__(self, position, value):
        self.value=value
        self.position=position
    def getPosition(self):
        return self.position
    def getvalue(self):
        return self.value
    def getNodeHash(self):
        return hash(str(self.position)+str(self.value))
    def __str__(self):
        return str('Pos:'+str(self.position)+' Val:'+str(self.value))
```

```

class edge(object):
    def __init__(self,src,dest):
        self.src = src
        self.dest = dest
    def getSource(self):
        return self.src
    def getDestination(self):
        return self.dest
    def getWeight(self):
        return self.dest.getvalue()
    def __str__(self):
        return str(self.src.getPosition())+'-->'+str(self.dest.getPosition())

class emap(object):
    def __init__(self):
        self.edges = {}
    def addNode(self,node):
        if node in self.edges:
            raise ValueError('Duplicate node')
        else:
            self.edges[node]=[]
    def addEdge(self,edge):
        src = edge.getSource()
        dest = edge.getDestination()
        if not (src in self.edges and dest in self.edges):
            raise ValueError('Node not in graph')
        self.edges[src].append(dest)
    def getChildrenof(self,node):
        return self.edges[node]
    def hasNode(self,node):
        return node in self.edges
    def display(self):
        for i in self.edges:
            print(i)
    def getedgelen(self):
        return len(self.edges)

class defect_map(object):
    def __init__(self):
        self.len=0
        self.images = []
        self.imsiz = []
        self.density = []
    def addimage(self,im,siz):
        self.images.append(im)
        self.imsiz.append(siz)
        self.len += 1
    def getlen(self):
        return self.len
    def select_defects(self, win):

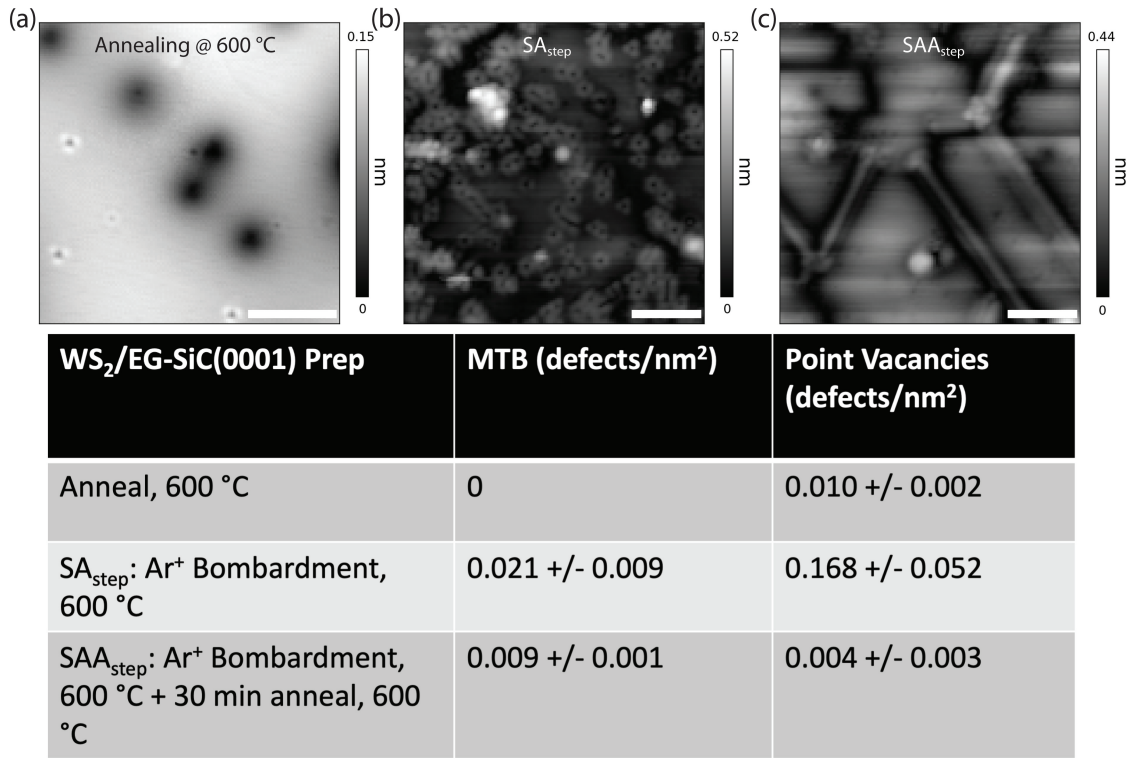
```

```

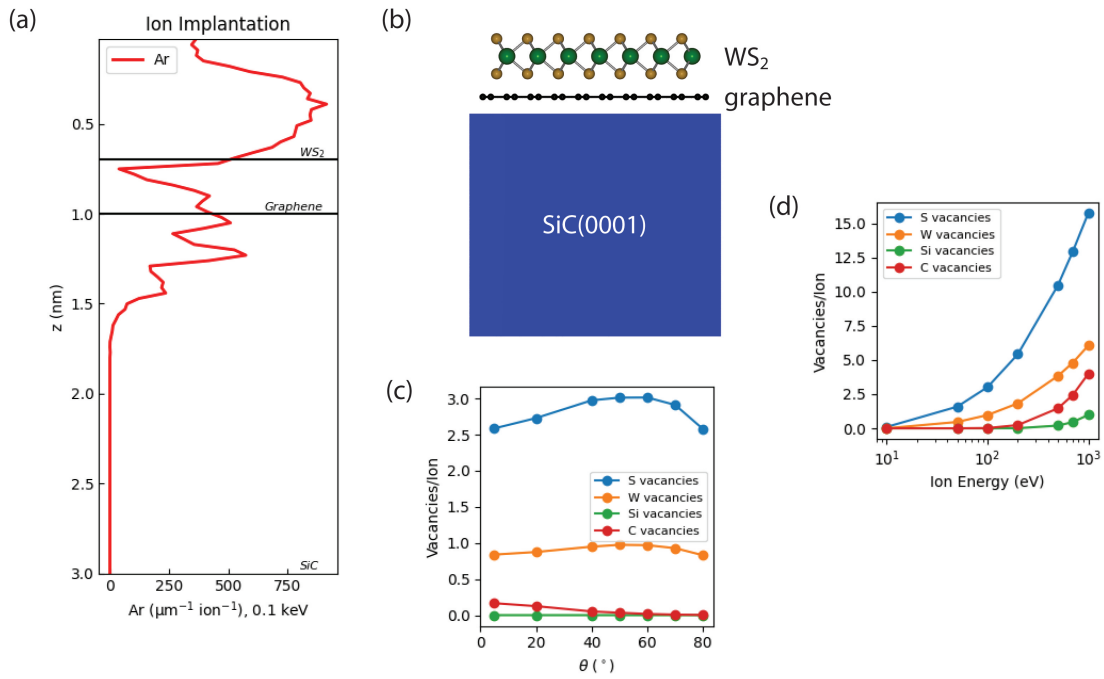
for idx in range(0,len(self.images)):
    outpts = selectdefects(self.images[idx],win,idx)
    dList = emap()
    nlist = []
    k = 0
    for x, y, z in outpts:
        mol=node([x,y],k)
        dList.addNode(mol)
        nlist.append(mol)
        k += 1
    visited = []
    for i in nlist:
        visited.append(i)
        for j in nlist:
            if j not in visited:
                dList.addEdge(edge(i,j))
    self.density.append(dList.getedgelen())
def getdensity(self):
    tmp = []
    for i in range(0,len(self.density)):
        tmp.append(self.density[i]/(self.imsz[i]**2))
    return tmp

```

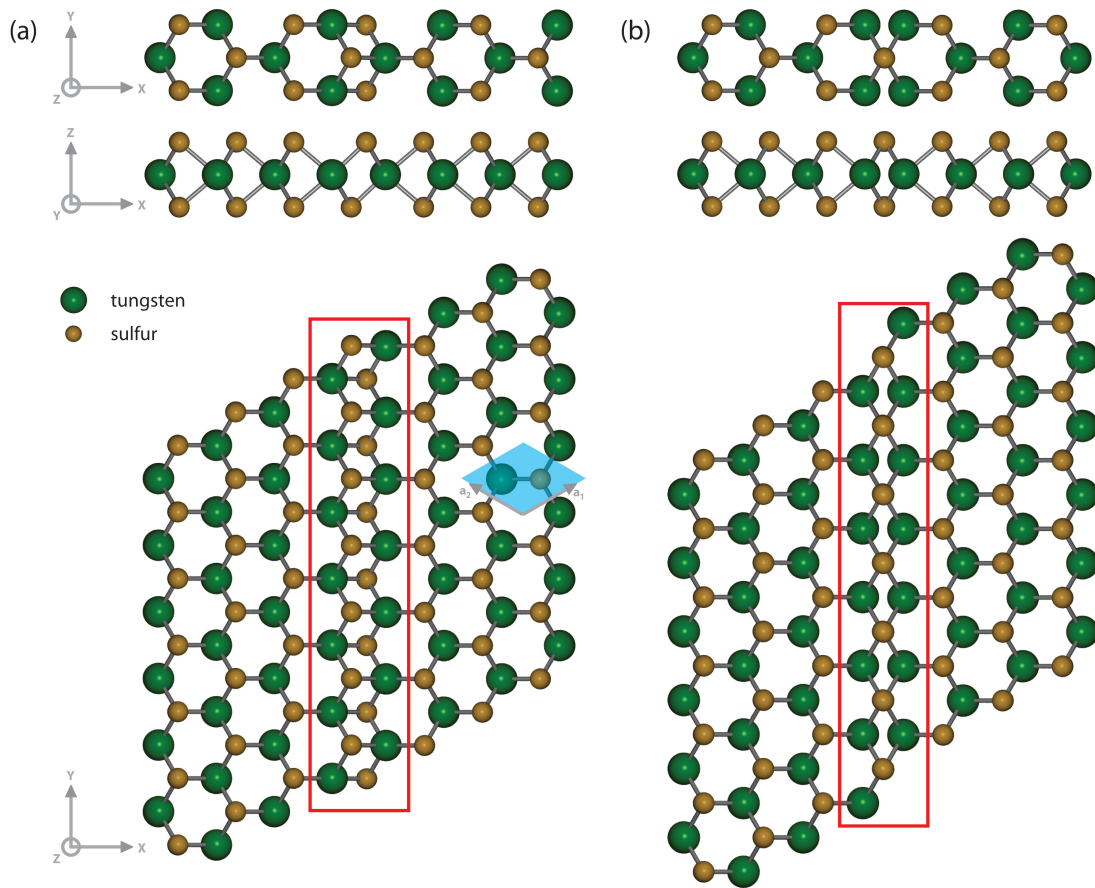

SUPPLEMENTARY FIGURES



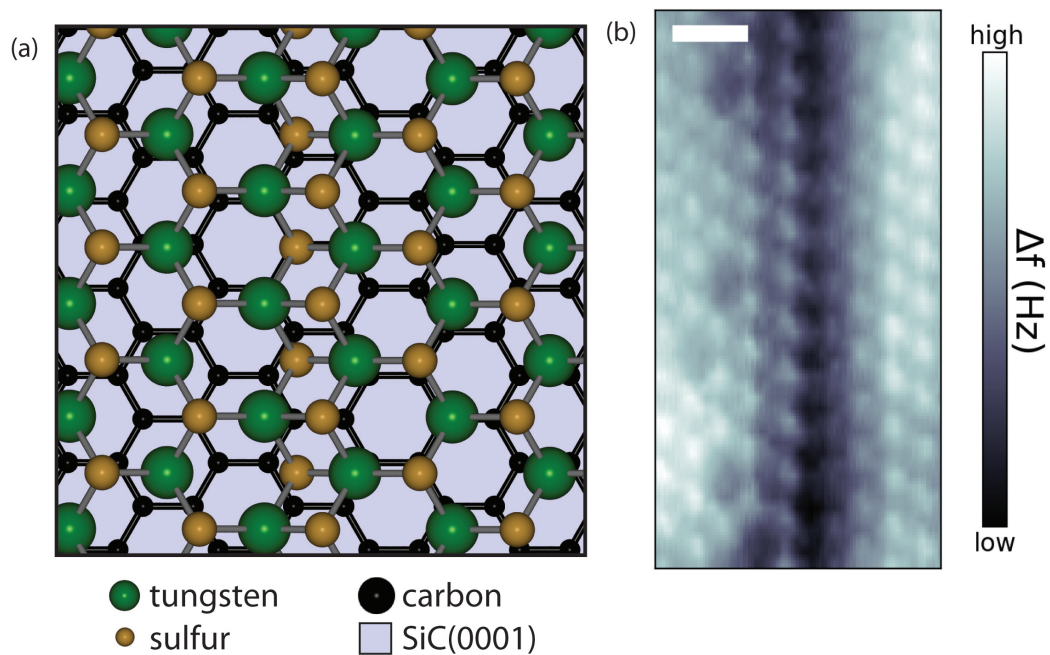
Supplementary Fig. 1: **Defect Density.** Defective density is calculated as the number of defects per unit area, where (a) annealed only samples show a low defect density, (b) sputtered with annealing produces a larger number of both MTBs and V_S , and (c) sputtered with annealing plus an additional 30 minute anneal produces elongated MTBs with less V_S ($I_{tunnel} = 30$ pA, $V_{sample} = 1.2$ V). Scale bars, 4 nm. Each defect, across a large number of images over multiple samples and subsequent preparations, is selected by inspection and then by solving for the local minima or maxima within a given pixel window.



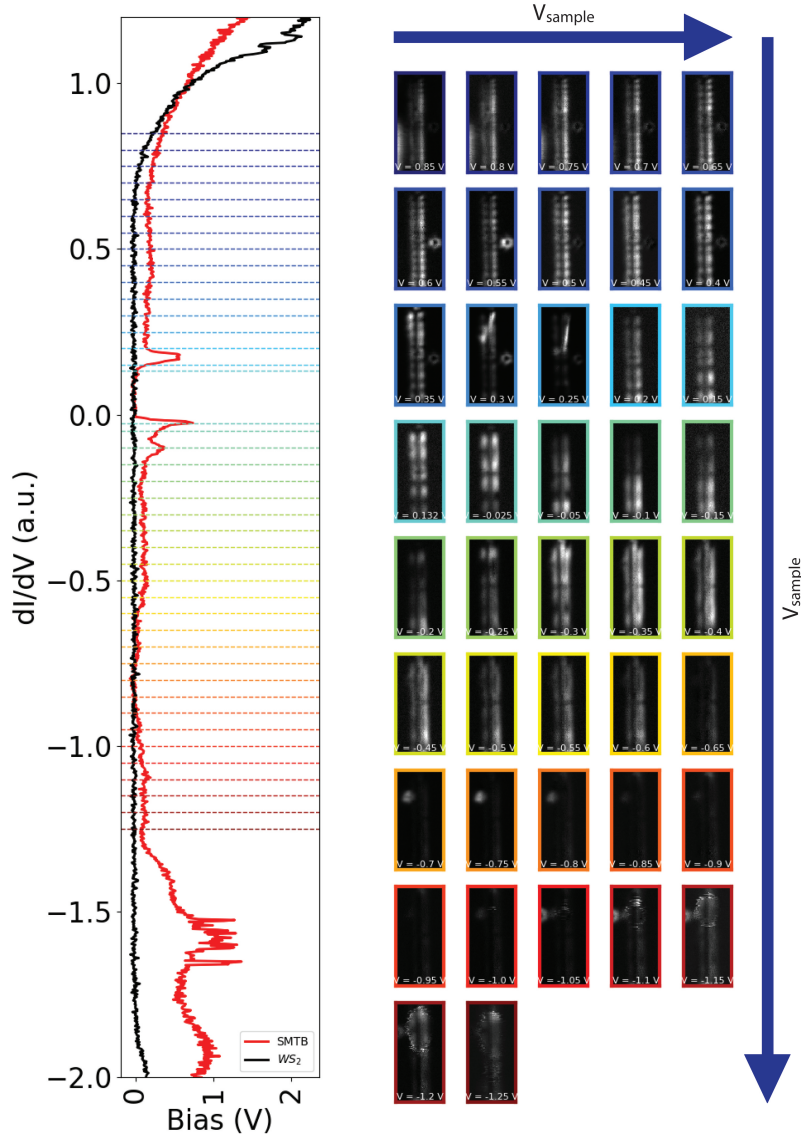
Supplementary Fig. 2: **SRIM Simulations.** (a) Results of SRIM simulations with 50000 ions for a (b) WS_2 /Graphene/SiC(0001) heterostructure, where Ar^+ ions are expected to nominally interact with the TMD overlayer given the ion energy and angle of irradiation incidence. Both (c) and (d) depict the number of vacancies produced over a given incidence angle and energy, where we use an energy of 0.1 keV and an angle of 60° , respectively.



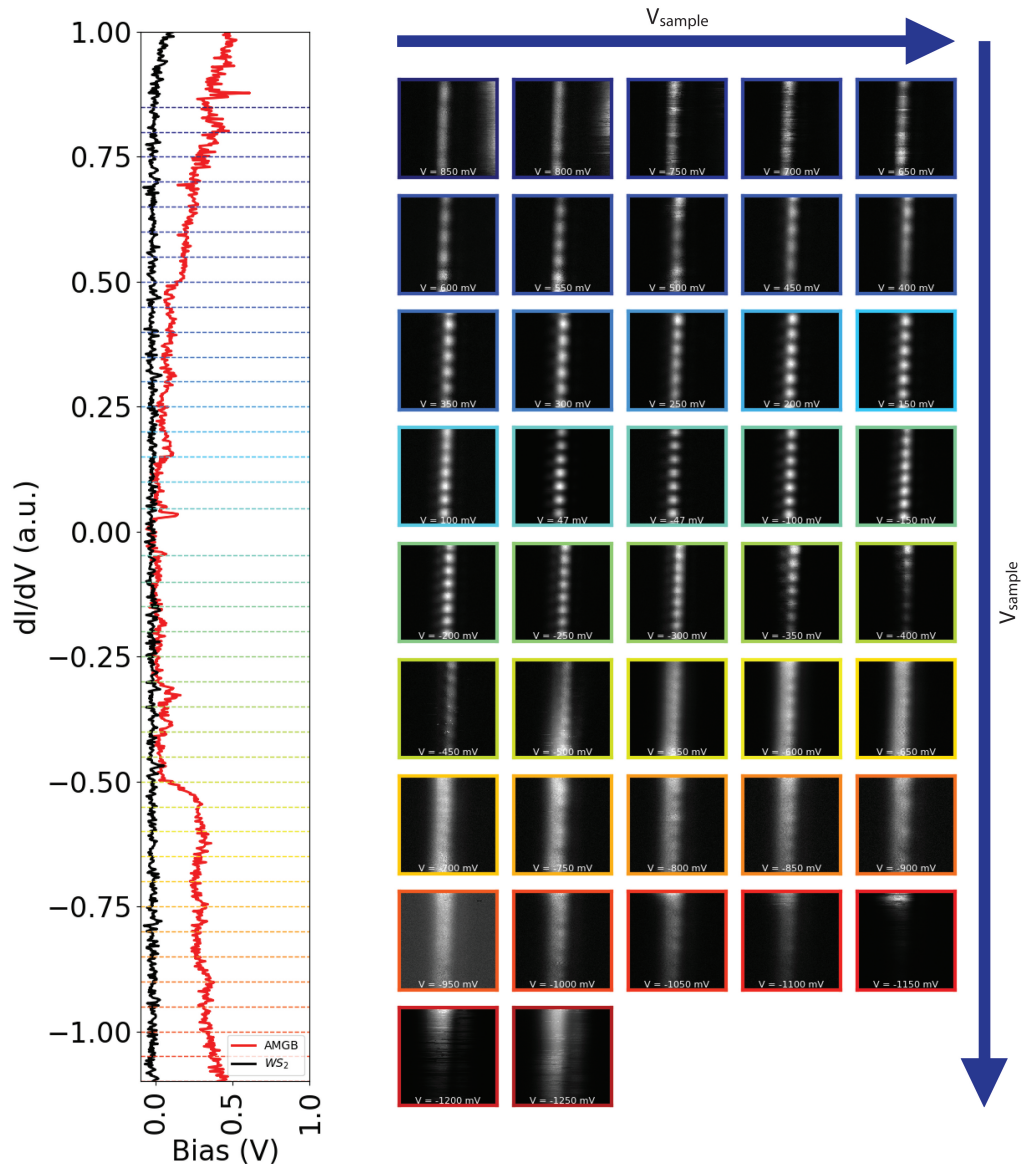
Supplementary Fig. 3: **MTB Structure.** (a) AMGB (or 4|4E) structure shown in both the z and y directions, where the MTB, described by an edge shifted by $\frac{1}{2}a$ ($a=a_1=a_2$), is highlighted in red. (b) The SMTB (or 4|4P) structure shown in both the z and y directions, which is connected at chalcogen site link with opposing tungsten atoms, is highlighted in red for clarity.



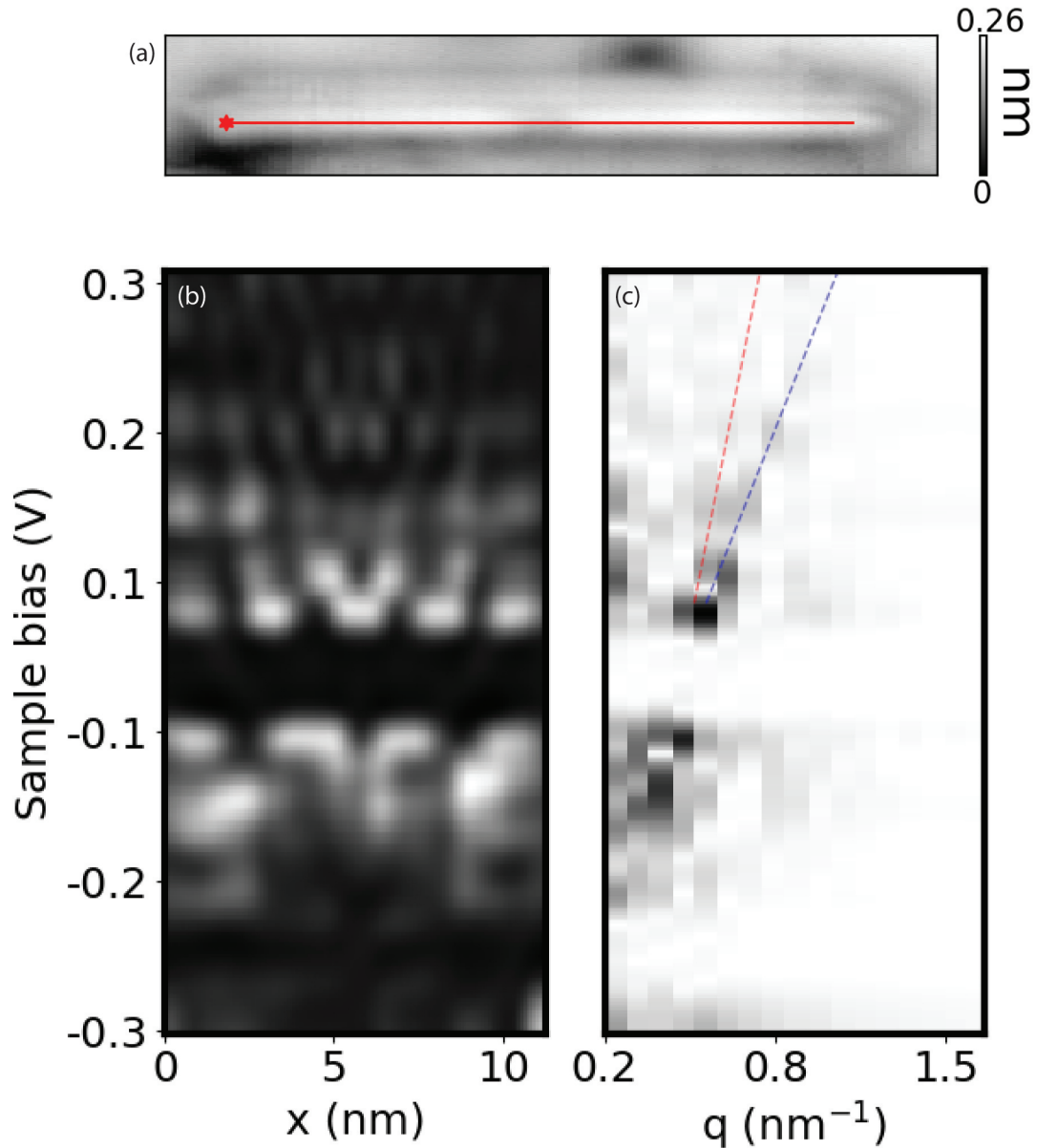
Supplementary Fig. 4: **Atomic Force Imaging.** (a) Schematic depicting the AMGB over graphene that is collected by (b) ncAFM with a CO functionalized tip ($V_{sample} = 0.0$ V). Scale bar, 0.25 nm. Depressions near the AMGB reflect oxygen atoms within an otherwise unmodified WS₂ lattice.



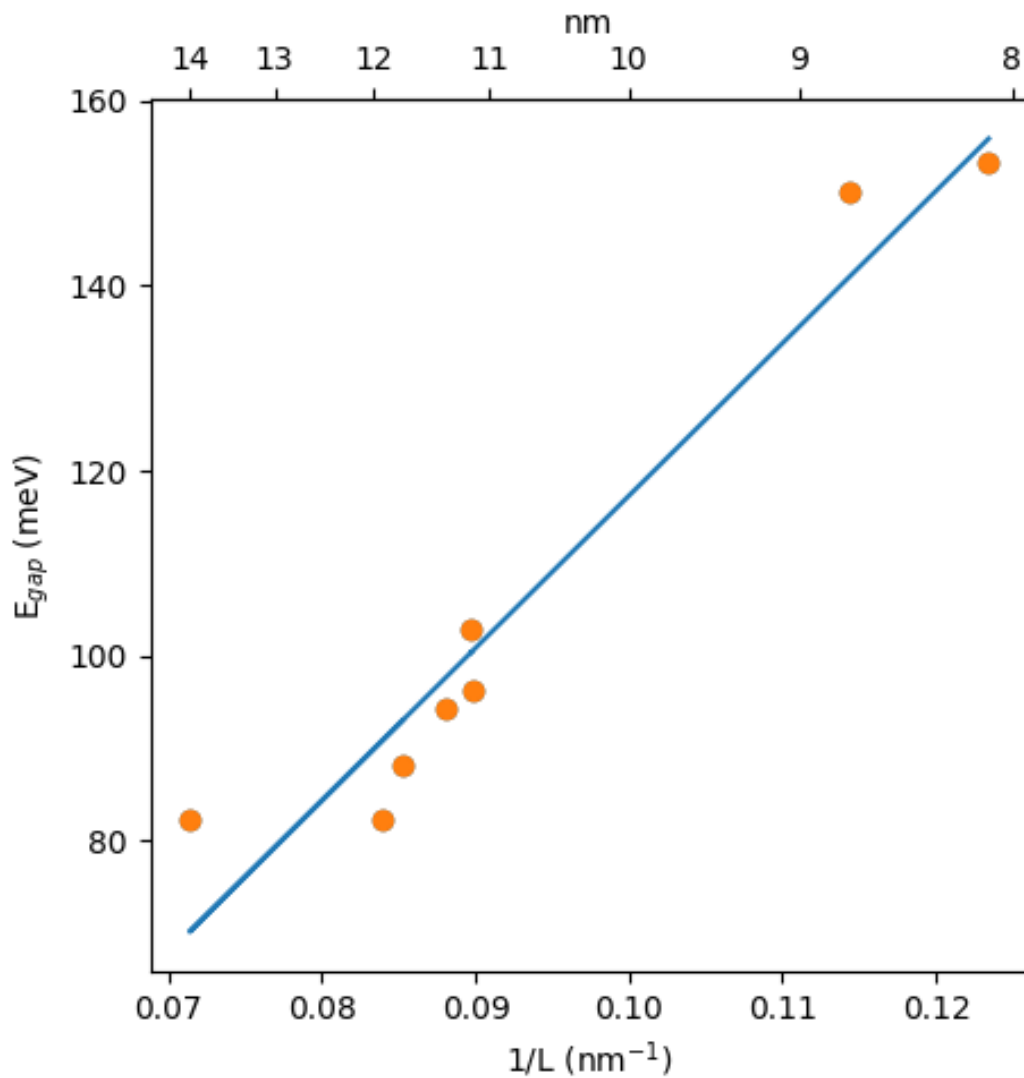
Supplementary Fig. 5: **Differential Conductance Mapping.** dI/dV mapping ($V_{modulation} = 5$ mV) over the spectra region shown for an SMTB on a jet color scale, where the energy is ramped from near the VBM of WS_2 by 0.05 V to the HOS gap opening of the MTB hosting a TLL, and then from the LUS to the CBM of WS_2 . Arrows indicate decreasing bias. A 1D particle in a box behavior is evident, and orbitals of both the TLL and a V_S can be visualized at respective energies.



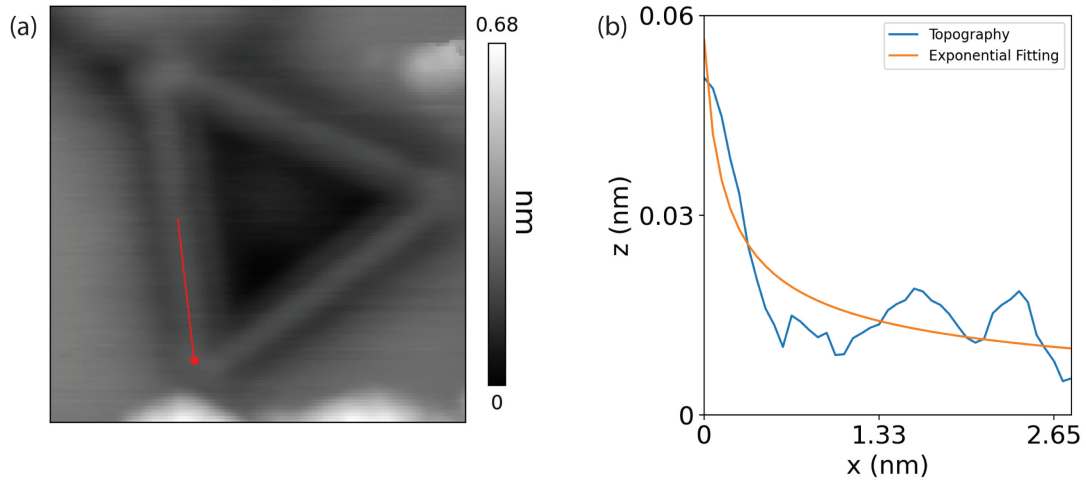
Supplementary Fig. 6: **Differential Conductance Mapping.** dI/dV mapping ($V_{modulation} = 5$ mV) over the spectra region shown for an AMGB on a jet color scale, where the energy is ramped from near the VBM of WS_2 by 0.05 V to the HOS, and then from the LUS to the CBM of WS_2 . Orbitals of the as-formed TLL can be visualized as a function of bias voltage, where arrows indicate decreasing bias.



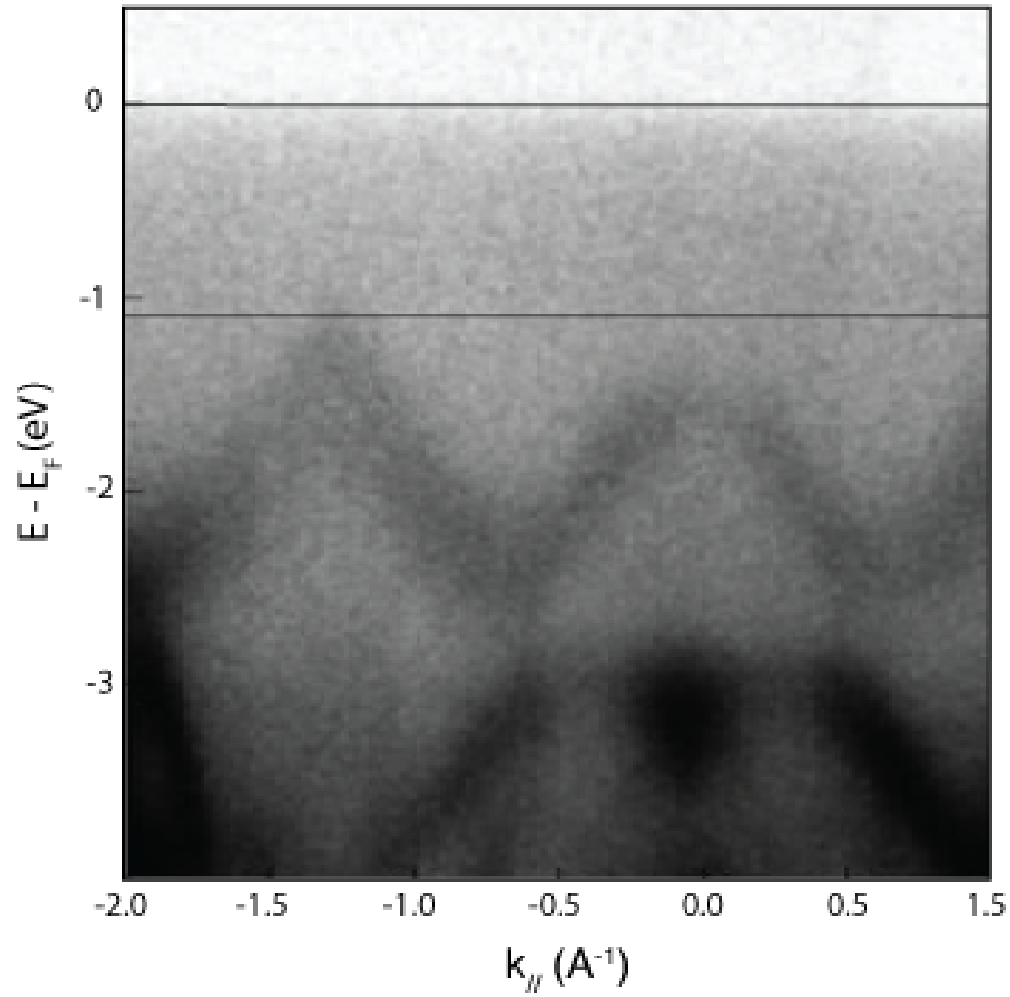
Supplementary Fig. 7: **Spatially Resolved Scanning Tunneling Spectroscopy.** Dense local density of states spectra collected along (a) an MTB (1x128x500 pixels) ($V_{modulation} = 5$ mV, $I_{set} = 150$ pA) beginning at the starred point along the red line. This is shown as a (b) function of bias and distance, where the (c) FT of this spectra gives rise to separate spin (blue) and charge (red) Fermi velocities. The relationship $K_c = \frac{v_s}{v_c}$ yields the Luttinger parameter of 0.5.



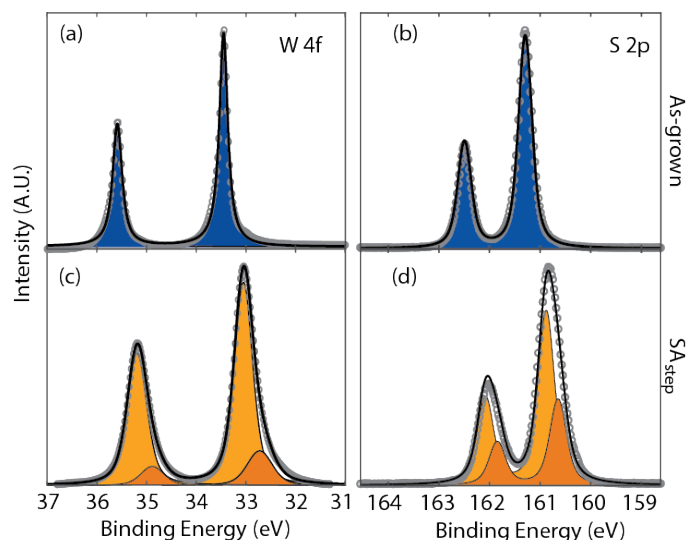
Supplementary Fig. 8: **Gap Length Dependence.** Band gaps are depicted across 8 MTBs, where each point represents the average of multiple reproducible data points, measured as a function of length (slope = 1644.9 ± 173.7 meV·nm, offset = -47.2 ± 16.4 meV). A linear relationship is shown across both SMTB and AMGB structures. Fitting was performed using the lmfit package in Python.⁷



Supplementary Fig. 9: **Constant-Current Density of States Decay Across an MTB.** A power law dependence is measured across a connected (a) MTB defect that starts at the starred point along the red line, where (b) the exponential fit, over an extracted region of high intensity to lower intensity, gives an exponential parameter matching the Luttinger parameter of 0.5. Fitting was performed using the lmfit package in Python.⁷



Supplementary Fig. 10: **nARPES Polarization Investigation.** WS₂ bands collected with linear vertical polarization. The horizontal line below $E - E_F$ indicate the top of the valence band for the defective crystal.



Supplementary Fig. 11: **Measured W and S Core Levels Spectra of As-grown and Defective WS₂**. (a) W 4*f* 7/2 and 5/2 levels centered at 33.5 eV and 35.7 eV, respectively, and (b) S 2*p* 3/2 and 1/2 core levels centered at 161.3 eV and 162.4 eV, respectively, from the unmodified sample. (c) and (d) are relative to WS₂ after SA_{step}, displaying two components (light and dark orange), with a relative shift of 0.4 eV for W 4*f* peaks and 0.2 eV for S 2*p* peaks.

REFERENCES

- [1] Ziegler, J. F., Ziegler, M., & Biersack, J. SRIM – The stopping and range of ions in matter. *Nucl. Instrum. Methods Phys. Res. B: Beam Interact. Mater. At.* **268**, 1818 (2010).
- [2] Mitterreiter, E. et al. The role of chalcogen vacancies for atomic defect emission in MoS₂. *Nat. Commun.* **12**, 3822 (2021).
- [3] Fox, D. et al. Helium ion microscopy of graphene: beam damage, image quality and edge contrast. *Nanotechnology* **24**, 335702 (2013).
- [4] Komsa, H.-P. et al. Two-dimensional transition metal dichalcogenides under electron irradiation: Defect production and doping. *Phys. Rev. Lett.* **109**, 035503 (2012).
- [5] Susi, T. et al. Isotope analysis in the transmission electron microscope. *Nat. Commun.* **7**, 13040 (2016).
- [6] Chang, J., Cho, J.-Y., Gil, C.-S., & Lee, W.-J. A simple method to calculate the displacement damage cross section of silicon carbide. *Nucl. Eng. Technol.* **46**, 475 (2014).
- [7] Newville, M., Stensitzki, T., Allen, D. B., & Ingargiola, A. LMFIT: Non-Linear Least-Square Minimization and Curve-Fitting for Python. <https://lmfit.github.io/lmfit-py/> (2014).